

A Mathematical Model for Reactions During Top-Blowing in the AOD Process: Derivation of the Model



VILLE-VALTTERI VISURI, MIKA JÄRVINEN, AKI KÄRNÄ, PETRI SULASALMI, EETU-PEKKA HEIKKINEN, PENTTI KUPARI, and TIMO FABRITIUS

In an earlier work, a fundamental mathematical model was proposed for side-blowing operation in the argon–oxygen decarburization (AOD) process. The purpose of this work is to present a new model, which focuses on the reactions during top-blowing in the AOD process. The model considers chemical reaction rate phenomena between the gas jet and the metal bath as well as between the gas jet and metal droplets. The rate expressions were formulated according to a law of mass action-based method, which accounts for the mass-transfer resistances in the liquid metal, gas, and slag phases. The generation rate of the metal droplets was related to the blowing number theory. This paper presents the description of the model, while validation and preliminary results are presented in the second part of this work.

DOI: 10.1007/s11663-017-0960-6

© The Minerals, Metals & Materials Society and ASM International 2017

I. INTRODUCTION

THE argon–oxygen decarburization (AOD) process is the most common process for the refining of stainless steel.^[1] Owing to violent agitation caused by the high blowing rates, the AOD vessel has very good mixing characteristics.^[2–5] Nowadays, top-blowing is employed in conjunction with side-blowing in the early part of the decarburization stage in order to maximize oxygen delivery into the melt.^[6] As illustrated in Figure 1, two main reaction areas can be identified during combined blowing: (1) inside the gas plume, and (2) on the surface of the bath, including metal droplets.^[7,8]

Numerous reaction models have been proposed for the decarburization^[8–37] and nitrification^[7,38–40] of steel in an AOD vessel. The majority of the models applicable for side-blowing decarburization have been reviewed elsewhere.^[21,41] Despite the vast number of reaction models available, there are only a few models that explicitly address the reactions during top-blowing in the AOD process. Arguably the most relevant examples found in the literature are those proposed by Watanabe and Tohge,^[9] Tohge *et al.*,^[17] Kikuchi *et al.*,^[23,42] and Wei *et al.*^[8,21,22,26,28] Some similarities in the modeling setting can be found in the reaction models proposed for the VOD process.^[41,43] To summarize, it can be stated that the top-blowing models proposed so far are capable of predicting the decarburization with a reasonable

degree of accuracy and have laid the basic foundations for further investigations. However, more research is required along these lines in order to obtain information on the related reaction interfaces and chemical reaction rate phenomena.

In our previous work,^[29,30] a fundamental model was proposed and validated for the reactions inside the bath during side-blowing in the AOD process. Consequently, the aim of this work was to extend the original model by developing a mathematical model for reactions during top-blowing. In order to provide more information on the controlling mechanisms and dynamics of decarburization during top-blowing, the model combines the transient solution of multicomponent equilibria with a description of the constraining mass transfer. This paper presents the description of the model, while validation and preliminary results are presented in the second part of this work.^[44]

II. DERIVATION OF THE MODEL

The model was programmed using C++, and the main assumptions can be summarized as follows:

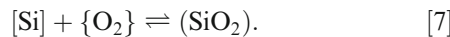
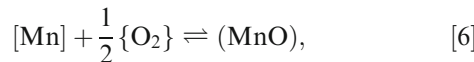
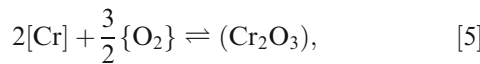
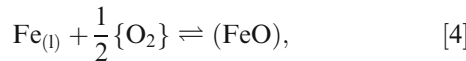
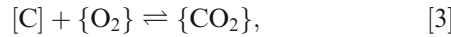
1. The top-blown oxygen may react with iron and the species dissolved in iron, dissolve in the metal bath, or escape through the gas exit.
2. Reactions between gas, metal, and slag species take place simultaneously at the surface of the cavity as well as at surface of the metal droplets generated due to top-blowing.
3. Owing to the high temperature, the reaction rates are assumed to be limited by mass transfer onto and from the reaction interfaces, and hence the reaction interfaces are able to reach their constrained thermodynamic equilibrium at any given moment.
4. Conservation of mass and heat is solved successively.

VILLE-VALTTERI VISURI, AKI KÄRNÄ, PETRI SULASALMI, EETU-PEKKA HEIKKINEN, and TIMO FABRITIUS are with the Process Metallurgy Research Unit, University of Oulu, PO Box 4300, 90014 University of Oulu, Finland. Contact e-mail: ville-valtteri.visuri@oulu.fi MIKA JÄRVINEN is with the Department of Mechanical Engineering, Aalto University, PO Box 14440, 00076 Aalto, Finland. PENTTI KUPARI is with the Outokumpu Stainless Oy, 95490 Torne, Finland.

Manuscript submitted June 11, 2015.

Article published online March 27, 2017.

The liquid metal phase is assumed to consist of Fe as the solvent and Cr, Mn, Si, C, O, N, Ni, Al, and S as solutes. The gas phase consists of O₂, CO, CO₂, N₂, and Ar. The slag phase consists of FeO, Cr₂O₃, MnO, SiO₂, CaO, MgO, Al₂O₃, CaF₂, and MeO_x, which is a generic oxide and depicts the residual species. The reaction system considered is defined by the following reactions:



The rate expressions were formulated as reversible according to a modified Law of Mass Action, a method that has been discussed more comprehensively in our earlier work.^[45,46] More specifically, the rate expressions are defined such that concentrations are replaced with activities and partial pressures, as illustrated below for the oxidation of the dissolved carbon to carbon monoxide:

$$R'' = k_f \left(a_{[\text{C}]} p_{\text{O}_2}^{1/2} - \frac{p_{\text{CO}}}{K} \right), \quad [8]$$

where k_f is the forward reaction rate coefficient, $a_{[\text{C}]}$ is the activity of dissolved carbon, p_{O_2} is the partial pressure of gaseous oxygen, and K is the equilibrium constant.

A. Conservation of Mass

The observed system consists of gas input, gas exit, two reaction interfaces, and three bulk volumes, as shown in Figure 2. It should be noted that the reaction interfaces have neither thickness nor mass.

It has been proposed that during simple side-blowing, post-combustion takes place in the off-gas flue, but not in the AOD vessel itself.^[47] However, during combined top- and side-blowing, a part of the top-blown oxygen may be consumed in the post-combustion of CO to CO₂ before the gas jet impacts the bath surface.^[8] In order to

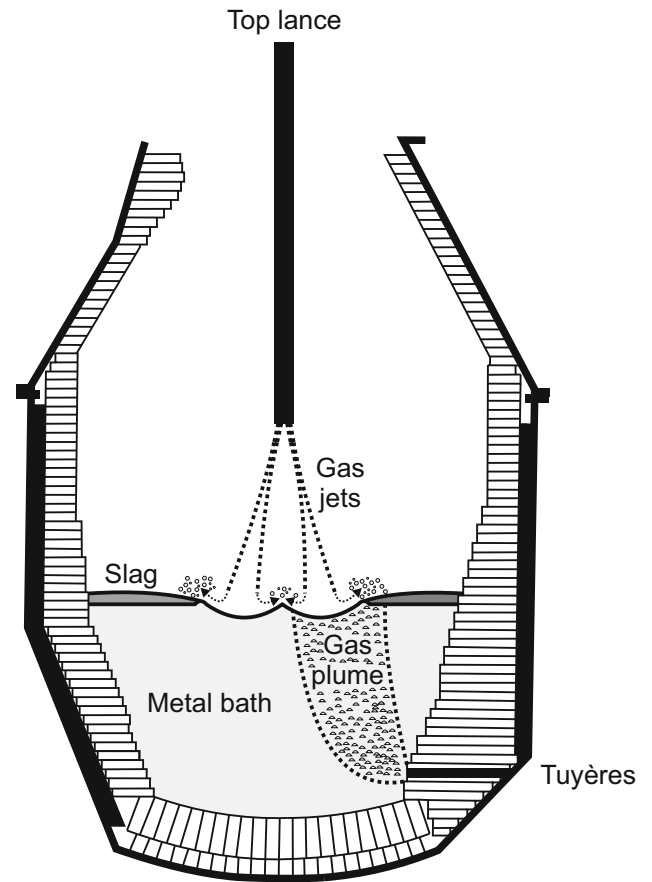


Fig. 1—Schematic illustration of combined blowing in an AOD vessel.

simplify the modeling setting, the model proposed in this paper considers post-combustion only at the reaction interfaces. Because the entrainment of cold air from the atmosphere outside the vessel can be neglected under normal operating conditions,^[48] the top-lance and the tuyères can be taken as the only gas inputs of the system. More specifically, it was assumed that the side-blown gas exits the metal bath through the plume eye and comes into contact with the top-blown gas. The mass flow of gaseous species through the top lance into the observed system is given by

$$\dot{m}_{\text{G,in,lance}} = \dot{V}_{\text{G,lance}} \rho_{\text{G,STP}}, \quad [9]$$

where $\dot{V}_{\text{G,lance}}$ is the volumetric gas flow rate through top lance (in Nm³/s) and $\rho_{\text{G,STP}}$ is the density of the gas mixture under standard temperature and pressure according to the DIN 1343 standard^[49]: 273.15 K (0 °C) and 101325 Pa. The model is coupled with the earlier-proposed model for side-blowing decarburization,^[29] which calculates the mass flow of gaseous species from the plume eye (into the observed system). In the case of inert gases, the mass flow rate of gas from the plume eye is equal to the mass flow rate of gas from the tuyères. Preventing the suction of atmospheric gas, the mass flux of gas exiting the system is obtained from

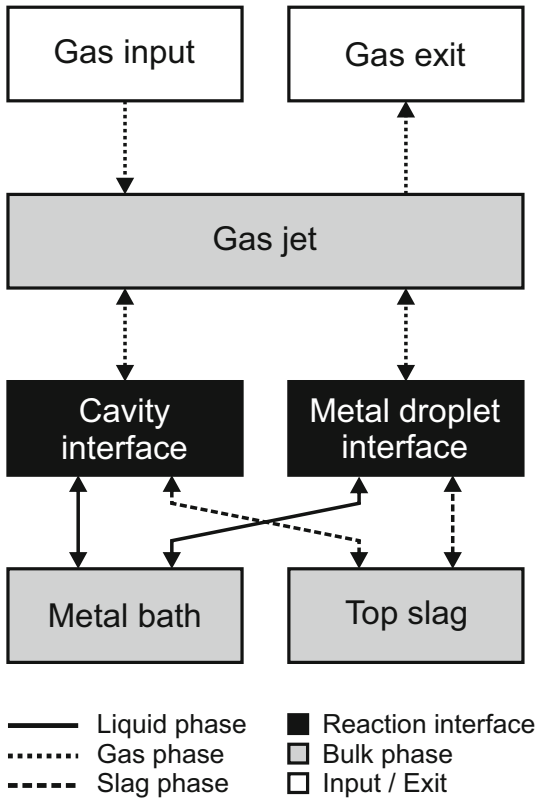


Fig. 2—Schematic illustration of the interaction of the reaction interfaces.

$$\dot{m}_{G,\text{out}} = \max \left(\underbrace{\dot{m}_{G,\text{in,lance}} + \dot{m}_{G,\text{in,plume}}}_{\text{gas injection}} - \underbrace{\dot{m}_{G,\text{cav}} + \dot{m}_{G,\text{md}}}_{\text{gas consumption}}, 0 \right), \quad [10]$$

where $\dot{m}_{G,\text{in,plume}}$ is the mass flow of gas from the plume eye, $\dot{m}_{G,\text{cav}}$ is the mass flow of gas from the cavity interface, and $\dot{m}_{G,\text{md}}$ is the mass flow of gas from the metal droplet interface. In order to avoid the mathematical complexity of the Maxwell–Stefan equations and the generalized Fick’s law, an effective diffusion model was employed.^[50] The conservation of species at the two reaction interfaces is defined by the reaction rates and mass-transfer rates onto and from the reaction surfaces. Employing a first-order upwind scheme for the Stefan flow, the conservation of species i in phase ψ at reaction interface ω is given by

$$\underbrace{\beta_{i,\psi,\omega} \rho_{\psi,\omega} (y_{i,B} - y_{i,\omega}^*)}_{\text{mass transport}} + \underbrace{\max(m''_{\psi,\omega}, 0) y_{i,B} - \max(-m''_{\psi,\omega}, 0) y_{i,\omega}^*}_{\text{Stefan flow}} + \underbrace{\sum_{k=1}^r R''_{k,\omega} \bar{v}_{i,k}}_{\text{chemical reactions}} = 0, \quad [11]$$

where β is the mass-transfer coefficient, ρ is the density, $y_{i,B}$ is the mass fraction of species i in the bulk phase (i.e., metal bath, gas jet, or top slag), $y_{i,\omega}^*$ is the interfacial mass fraction of species i , m'' is the total mass flux, R'' is the reaction rate, and \bar{v} is the mass-based stoichiometric coefficient. It should be noted that all properties are specific to the reaction interface in question. In order to account for conservation of mass within the metal droplets, the following expression is employed for species in the metal phase at the metal droplet interface:

$$\underbrace{\left(\frac{m_{\text{md}}}{A_{\text{md}} \bar{t}_{\text{md}}} - m''_{L,\text{md}} \right) \bar{\eta}_{i,M,\text{md}} (y_{i,\text{bath}} - y_{i,\text{md}}^*)}_{\text{mass transport}} + \underbrace{m''_{L,\text{md}} y_{i,\text{bath}}}_{\text{Stefan flow}} + \underbrace{\sum_{k=1}^r R''_{k,\text{md}} \bar{v}_{i,k}}_{\text{chemical reactions}} = 0, \quad [12]$$

where m_{md} , A_{md} , and \bar{t}_{md} are the mass, surface area, and average residence time of the metal droplets, respectively, and $\bar{\eta}_{i,M,\text{md}}$ is the average microkinetic efficiency for mass transfer of species i in the metal droplets. The total mass flux of the metal phase is subject to the constraint $m''_{L,\text{md}} \leq \frac{m_{\text{md}}}{A_{\text{md}} \bar{t}_{\text{md}}}$. The average microkinetic efficiency was calculated based on the average residence time of the metal droplets:

$$\bar{\eta}_{i,M,\text{md}} = \frac{y_{i,\text{bath}} - y_{i,\text{md}}}{y_{i,\text{bath}} - y_{i,\text{md}}^*} = 1 - \exp \left(-\beta_{i,L,\text{md}} \frac{A_{\text{md}}}{V_{\text{md}}} \bar{t}_{\text{md}} \right), \quad [13]$$

where $y_{i,\text{md}}$ is the composition of species i in the metal droplets. The mass-based stoichiometric coefficients $\bar{v}_{i,k}$ are defined in relation to key components:

$$\bar{v}_{i,k} = v_{i,k} \frac{M_i}{M_{K,k}}, \quad [14]$$

where $v_{i,k}$ is the stoichiometric coefficient of species i in reaction k , $M_{K,k}$ is the molar mass of the key component of reaction k , and M_i is the molar mass of species i . The key components of the reactions shown in Eqs. [1] through [7] are O₂, C, C, Fe, Cr, Mn, and Si, respectively. The total mass flux of phase ψ at reaction interface ω is given by

$$m''_{\psi,\omega} = - \sum_{i=1}^n \sum_{k=1}^r \Gamma_{i,\psi} R''_{k,\omega} \bar{v}_{i,k}, \quad [15]$$

where $\Gamma_{i,\psi}$ is a binary operator, which is defined as 1 if species i is in phase ψ and 0 otherwise. The total mass flows $\dot{m}_{\psi,\omega}$ are obtained by multiplying the mass flux $m''_{\psi,\omega}$ by the corresponding interfacial area A_{ω} . Employing the implicit Euler method for time integration, the conservation of species i in the metal bath, top-blown gas, and top slag is defined by Eqs. [16] through [18], respectively.

$$\begin{aligned}
& -\beta_{i,L,cav}\rho_{L,cav}A_{cav}(y_{i,bath}-y_{i,cav}^*)-\max(m''_{L,cav},0)A_{cav}y_{i,bath} \\
& +\max(-m''_{L,cav},0)A_{cav}y_{i,cav}^* \\
& -\left(\frac{m_{md}}{\bar{t}_{md}}-m''_{L,md}A_{md}\right)\bar{\eta}_{i,M,md}(y_{i,bath}-y_{i,md}^*) \\
& -m''_{L,md}A_{md}y_{i,bath}-\frac{m_{bath}y_{i,bath}-m_{bath}^{t-\Delta t}y_{i,bath}^{t-\Delta t}}{\Delta t}=0
\end{aligned} \tag{16}$$

$$\begin{aligned}
& \sum_{\omega}\left[-\beta_{i,G,\omega}\rho_{G,\omega}A_{\omega}(y_{i,jet}-y_{i,\omega}^*)-\max(m''_{G,\omega},0)A_{\omega}y_{i,jet}\right. \\
& \left.+\max(-m''_{G,\omega},0)A_{\omega}y_{i,\omega}^*\right]+\dot{m}_{G,in,lance}y_{i,in,lance} \\
& +\dot{m}_{G,in,plume}y_{i,in,plume}-\dot{m}_{G,out}y_{i,jet} \\
& -\frac{m_{jet}y_{i,jet}-m_{jet}^{t-\Delta t}y_{i,jet}^{t-\Delta t}}{\Delta t}=0,
\end{aligned} \tag{17}$$

$$\frac{m_{md}}{A_{md}\bar{t}_{md}}c_{p,L}\bar{\eta}_{H,md}(T_{bath}-T_{md}^*)+\alpha_{G,md}(T_{jet}-T_{md}^*)+\alpha_{S,md}(T_{slag}-T_{md}^*)-\underbrace{\sum_{k=1}^r R''_{k,md}\Delta h_k}_{\text{chemical reactions}}=0 \tag{20}$$

$$\begin{aligned}
& \sum_{\omega}\left[-\beta_{i,S,\omega}\rho_{S,\omega}A_{\omega}(y_{i,slag}-y_{i,\omega}^*)-\max(m''_{S,\omega},0)A_{\omega}y_{i,slag}\right. \\
& \left.+\max(-m''_{S,\omega},0)A_{\omega}y_{i,\omega}^*\right]-\frac{m_{slag}y_{i,slag}-m_{slag}^{t-\Delta t}y_{i,slag}^{t-\Delta t}}{\Delta t}=0,
\end{aligned} \tag{18}$$

where m_{bath} , m_{jet} , and m_{slag} are the masses of the metal bath, gas jet, and top slag, respectively; and Δt is the time step. The conservation equations for the total mass of the bulk phases (for the metal bath, gas jet, and top slag) are defined correspondingly by summation of the mass transport terms and fluxes of species that are relevant to the bulk phase in question. Metal losses to dust were not accounted for as their effect on the composition of the metal bath is negligible.

B. Conservation of Heat

Temperature increase is defined by the difference in heat generation and heat losses. While heat is generated by exothermic reactions, it is consumed by

endothermic reactions as well as heat losses through the refractory lining, and top slag, and exiting gas. The conservation of heat at the cavity interface is defined according to

$$\begin{aligned}
& \underbrace{\alpha_{L,cav}(T_{bath}-T_{cav}^*)+\alpha_{G,cav}(T_{jet}-T_{cav}^*)+\alpha_{S,cav}(T_{slag}-T_{cav}^*)}_{\text{heat transport}} \\
& -\underbrace{\sum_{k=1}^r R''_{k,cav}\Delta h_k}_{\text{chemical reactions}}=0
\end{aligned} \tag{19}$$

where α is the heat-transfer coefficient, T_{bath} is the temperature of the metal bath, T_{cav}^* is the temperature of the cavity reaction interface, T_{jet} is the temperature of the gas jet, and Δh_k is the specific reaction enthalpy of reaction k . The conservation of heat at the metal droplet interface was defined according to where T_{md}^* is the interfacial temperature of the metal

droplets, and $\bar{\eta}_{H,md}$ is the average microkinetic efficiency of heat transfer in the metal droplets:

$$\bar{\eta}_{H,md}=\frac{T_{bath}-T_{md}}{T_{bath}-T_{md}^*}=1-\exp\left(-\alpha_{L,md}\frac{A_{md}}{m_{md}c_{p,L}}\bar{t}_{md}\right), \tag{21}$$

where T_{md} is the temperature of the metal droplets. Employing the implicit Euler method for time integration, the conservations of heat in the metal bath, in the top-blown gas, and in the top slag can be expressed according to Eqs. [22] through [24], respectively.

$$\begin{aligned}
& -\alpha_{L,cav}A_{cav}(T_{bath}-T_{cav}^*)-\frac{m_{md}}{\bar{t}_{md}}c_{p,L}\bar{\eta}_{H,md}(T_{bath}-T_{md}^*) \\
& -\sum_{\omega}\sum_{i=1}^n\sum_{k=1}^r\Gamma_{i,L}R''_{k,\omega}\bar{v}_{i,k}A_{\omega}c_{p,i}(T_{bath}-T_{\omega}^*) \\
& -q_{lining}A_{lining}-m_{bath}c_{p,bath}\frac{T_{bath}-T_{bath}^{t-\Delta t}}{\Delta t}=0,
\end{aligned} \tag{22}$$

$$\sum_{\omega} \left[-\alpha_{G,\omega} A_{\omega} (T_{\text{jet}} - T_{\omega}^*) - \sum_{i=1}^n \sum_{k=1}^r \Gamma_{i,G} R''_{k,\omega} \bar{v}_{i,k} A_{\omega} c_{p,i} (T_{\text{jet}} - T_{\omega}^*) \right] - \dot{m}_{G,\text{in},\text{lance}} \int_{T_{\text{in},\text{lance}}}^{T_{\text{jet}}} c_{p,\text{lance}} dT - \dot{m}_{G,\text{in},\text{plume}} \int_{T_{\text{plume}}}^{T_{\text{jet}}} c_{p,\text{plume}} dT - m_{\text{jet}} c_{p,\text{jet}} \frac{T_{\text{jet}} - T_{\text{jet}}^{t-\Delta t}}{\Delta t} = 0, \quad [23]$$

$$\sum_{\omega} \left[-\alpha_{S,\omega} A_{\omega} (T_{\text{slag}} - T_{\omega}^*) - \sum_{i=1}^n \sum_{k=1}^r \Gamma_{i,S} R''_{k,\omega} \bar{v}_{i,k} A_{\omega} c_{p,i} (T_{\text{slag}} - T_{\omega}^*) \right] - q_{\text{slag}} A_{\text{slag}} - m_{\text{slag}} c_{p,\text{slag}} \frac{T_{\text{slag}} - T_{\text{slag}}^{t-\Delta t}}{\Delta t} = 0, \quad [24]$$

where q_{lining} is the heat flux through the refractory lining, A_{lining} is the surface area of the refractory lining, q_{slag} is the heat flux through the slag, and A_{slag} is the cross-sectional surface area of the top slag. The values of A_{lining} and A_{slag} are calculated based on the geometry of the simulated converter. The heat flux through the refractory lining was set to $q_{\text{lining}} = 12,500 \text{ W/m}^2$ as in our previous work.^[29] The heat losses through the slag were determined on the basis of radiative heat transfer through the mouth of the vessel. Neglecting back-radiation, the radiative heat flux can be calculated as follows^[51]:

$$q_{\text{slag}} = \frac{\sigma T_{\text{slag}}^4}{\left[\frac{A_{\text{slag}} + A_{\text{mouth}} - 2A_{\text{slag}}F}{A_{\text{mouth}} - A_{\text{slag}}F^2} + \left(\frac{1}{\varepsilon_S} - 1 \right) \right]}, \quad [25]$$

where σ is the Stefan–Boltzmann constant; F is the view factor between the top slag and the converter mouth; A_{mouth} is the cross-sectional area of the vessel mouth; and ε_S is the emissivity of the slag phase, which was assumed to be $\varepsilon_S = 0.95$. The view factor for the top slag in relation to the vessel mouth is determined by^[51]

$$F = \frac{1}{2r_{\text{slag}}^2} \left[z^2 + r_{\text{slag}}^2 + r_{\text{mouth}}^2 - \left\{ \left(z^2 + r_{\text{slag}}^2 + r_{\text{mouth}}^2 \right)^2 - 4r_{\text{slag}}^2 r_{\text{mouth}}^2 \right\}^{1/2} \right], \quad [26]$$

where z is the distance between the top slag and the vessel mouth, r_{slag} is the radius of the top slag, and r_{mouth} is the radius of the vessel mouth. The cooling effect of the side-blown gas on the metal bath temperature is calculated separately by the earlier-proposed model for side-blowing decarburization^[29] and is not repeated here.

C. Geometry of the Cavity

The gas jet exits the lance nozzle at a supersonic velocity, but starts to spread and lose its velocity after

the supersonic core. The entrainment of gases from the ambient atmosphere affects the gas jet not only by decreasing its velocity, but also by increasing its mass flow, and—if the ambient temperature is higher than that of the gas jet—by increasing its temperature.^[52] Considering that the length of the supersonic region is typically 20 to 30 times the nozzle exit diameter at steelmaking temperatures,^[53] it is apparent that the gas jet impacts the surface of the metal bath at subsonic velocity. Upon impact, the momentum of the gas jet forms a cavity on the bath surface,^[53] while the liquid metal outside the cavity is pushed toward the refractory walls of the vessel in the radial direction.^[5]

Molloy^[54] distinguished three cavity modes, namely, dimpling, splashing, and penetrating. Dimpling refers to mere depression of the surface without droplet formation, while outwardly directed splashes start to form the edges of the depression when the mode changes to splashing. In the penetrating mode, the penetration depth is deeper, and outwardly directed splashes are reduced. The different modes can also be distinguished based on the frequency and amplitude of the cavity oscillation.^[55] Figure 3 presents a schematic illustration of the gas jet impact area with a one-hole lance in the splashing mode.

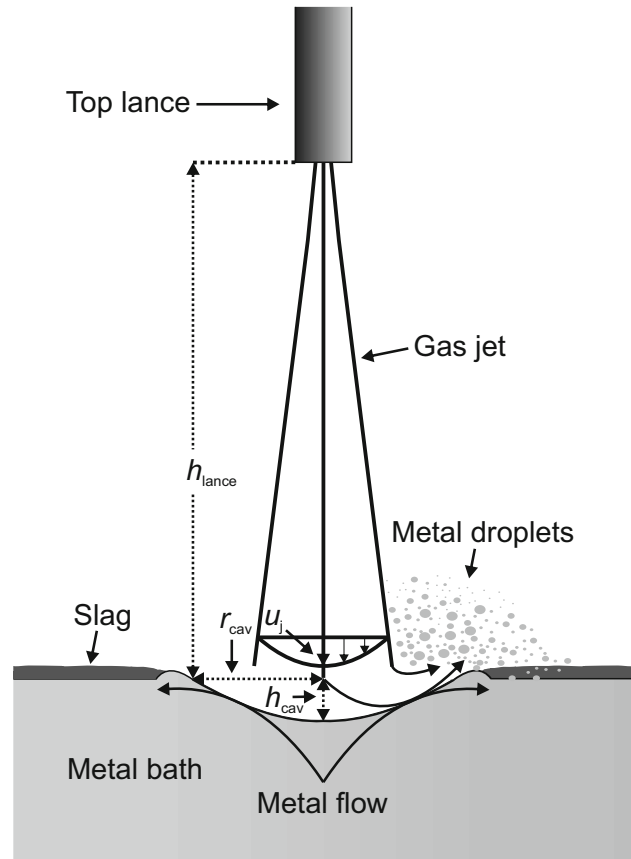


Fig. 3—Schematic illustration of the gas jet impact area with a one-hole lance.

In this work, the modeling setting was simplified by defining the reaction area between the gas jet and the metal bath as the surface area of the cavity. Because the surface of the cavity is in oscillating motion, the analysis must be based on quasi-steady-state flow conditions.^[53,56] It has been suggested that chemical reactions^[57,58] and the interference of top slag^[57] do not affect the geometry of the cavity to a significant extent and on this account their effect was excluded in this work. In accordance with Cheslak *et al.*,^[59] it was assumed that the geometry of the cavity follows the form of a paraboloid of revolution with an impact radius of r_{cav} and an impinging depth of h_{cav} (see Figure 3). The surface area of the paraboloid of revolution, excluding its base, can be calculated as follows^[60]:

$$A_{\text{cav},1} = \frac{\pi r_{\text{cav}}}{6 h_{\text{cav}}^2} \left[(r_{\text{cav}}^2 + 4h_{\text{cav}}^2)^{3/2} - r_{\text{cav}}^3 \right]. \quad [27]$$

For a three-hole lance, the geometry is slightly more complicated. Depending on the inclination angle of the gas jets, the gas jets may either coalesce and form only

one large cavity, or penetrate the bath surface as three separate jets, whereupon each gas jet will form its own cavity.^[61,62] Even if the gas jets do not coalesce, the cavities may still coalesce provided that they are sufficiently close to each other^[63] as shown in Figure 4. Observations with high-speed cameras^[64] suggest that the cavities remain noncoalescing when the inclination angle is greater than 10 deg. In this work, it is assumed that the gas jets do not coalesce and that the number of cavities is equal to the number of the gas jets (see Figure 4(a)). Therefore, the total surface area of the cavities caused by a multihole lance can be calculated simply by multiplying the surface area of a single cavity with the number of exit ports in the top lance^[52,65]:

$$A_{\text{cav}} = n_{\text{lance}} \times A_{\text{cav},1}. \quad [28]$$

The effects of various operating parameters on the depth and form of the cavity have been studied extensively. In this work, the correlations for the geometry of the cavity were taken from Koria and Lange.^[63] The equations required for calculating the depth and radius of the cavity are given in Table I. These are based on a dimensional analysis of experimental data on the penetration of oxygen jets in molten pig iron and pure iron-carbon alloys with both single- and multihole lances.^[63] It should be noted that Eq. [35] is applicable only for diatomic ideal gases (*e.g.*, O₂ or N₂) and their mixtures. For other gas mixtures, a more general expression for \dot{m}_t can be derived based on the equations presented by Koria.^[66]

D. Droplet Generation

The generation of metal droplets during top-blowing is important for steelmaking processes, because it brings about a considerable increase in the interfacial area available to chemical reactions.^[67] The contribution of metal droplets to the decarburization rate during top-blowing in the AOD process has been acknowledged likewise.^[7,8,23,42,68–70] However, foaming of the AOD slag does take place under typical operating conditions. Considering the high blowing rates and high viscosity of the slag, the behavior of slag should be somewhere

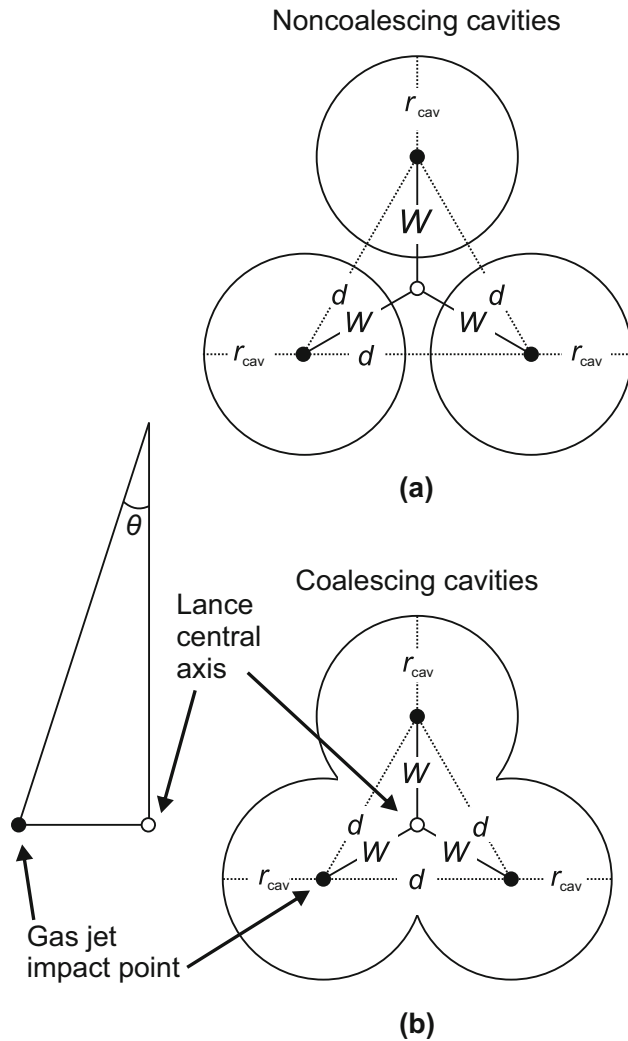


Fig. 4—Schematic illustration of the gas jet impact area with a 3-hole lance with noncoalescing (a) and coalescing (b) cavities.

Table I. Equations for Calculating the Geometry of the Cavity^[63]

Equation	Symbols
$h_{\text{cav}} = 4.469 \dot{M}_h^{0.66} h_{\text{lance}} [29]$	
$r_{\text{cav}} = 0.5 \times 2.813 \dot{M}_d^{0.282} h_{\text{lance}} [30]$	
$\dot{M}_h = \frac{\dot{m}_n \cos \theta}{\rho_L g h_{\text{lance}}^2} [31]$	
$\dot{M}_d = \frac{\dot{m}_t}{\rho_L g h_{\text{lance}}^2} (1 + \sin \theta) [32]$	A
$\dot{M}_d = \frac{n_{\text{lance}} \dot{m}_n \sin \theta}{\rho_L g h_{\text{lance}}^2} [33]$	B
$\dot{m}_n = \frac{\dot{m}_t}{n_{\text{lance}}} [34]$	
$\dot{m}_t = 0.7854 n_{\text{lance}} d_t^2 p_{\text{amb}} \left(1.27 \frac{p_0}{p_{\text{amb}}} - 1 \right) [35]$	C

A = diameter of a single cavity.
B = diameter of multiple cavities.
C = pressures in Pa.

between a void-free and an expanded slag. In such cases, the gas void fraction would depend on the gas velocity.^[71]

Different mechanisms contribute to generation of metal droplets. If the momentum flux of the top-blown gas jet is sufficiently high, the liquid surface becomes unstable and the splashing of metal droplets occurs.^[72] Standish and He^[73] identified two regions of droplet generation: *dropping* and *swarming*. In the dropping region, single droplets are gradually formed and ejected. This is the mechanism of droplet generation when the gas flow rate is relatively low. When the gas flow rate is increased past a certain limit, the system reaches the swarming region and the mechanism of droplet generation changes so that not only single droplets but also large tears of liquid phase are ejected from the bath. Generation of metal droplets is also caused by side-blowing through a mechanism referred to as bubble bursting.^[74–77] This phenomenon occurs when a rising gas bubble reaches the surface of the metal bath and bursts creating very small metal droplets from the thin film of metal around the bubble.^[74–77] A related mechanism is the entrainment of large droplets due to jet formation, which is caused by the collapsing of the cavity after the rupture of the iron film.^[76]

The secondary break-up of the metal droplets can occur due to various reasons, *e.g.*, due to the aerodynamic forces of the gas jet,^[78] impact on the slag layer^[79] or bursting resulting from spontaneous CO nucleation within the droplet.^[80] In the absence of suitable quantitative descriptions for the break-up mechanisms and due to uncertainties related to the trajectories of the droplets, the effect of the various break-up mechanisms on the droplet size distribution was not accounted for.

Based on the available knowledge, the lifespan of the metal droplets was assumed to consist of three successive steps. At first, the metal droplets are generated at the vicinity of the cavity, from which they are ejected onto a gas–metal–slag emulsion. This also includes metal droplets, which have been ejected into the atmosphere and land on the emulsion. Thereafter, the metal droplets pass through the emulsion layer, reacting simultaneously with gas and slag species. Finally, the metal droplets return to the metal bath, where they mix with the metal bath immediately. Based on experimental findings^[81] it was assumed that the initial composition of the metal droplets corresponds to the bulk composition. Furthermore, the metal droplets were assumed to be spherical in geometry. This assumption should hold well for small droplets,^[82] which are expected to form the majority of the surface area. Considering the distribution of emulsified metal droplets residing in the emulsion, their mass and surface area are obtained from the following equations:

$$m_{\text{md}} = \sum_i m_{\text{md},i}, \quad [36]$$

$$A_{\text{md}} = \sum_i \frac{6m_{\text{md},i}}{d_{\text{md},i}\rho_L}, \quad [37]$$

where $m_{\text{md},i}$ and $d_{\text{md},i}$ are the mass and diameter of the droplet size class i , respectively. As a matter of

practice, the droplet distribution was calculated from a diameter of 0.1 mm up to the diameter corresponding to the largest 99.9 pct by weight using a step size of 0.1 mm. The mass of droplets in the size class i residing in the emulsion can be solved from

$$m_{\text{md},i} = f_{\text{md},i} \dot{m}_{\text{md}} \min(t_{\text{md},i}, t), \quad [38]$$

where $f_{\text{md},i}$, \dot{m}_{md} and $t_{\text{md},i}$ are the mass fraction of size class i at place of birth, the metal droplet generation rate and the residence time of size class i , respectively, and t is the time. The Sauter mean diameter of the metal droplets residing in the emulsion at a given moment is obtained from

$$d_{32,\text{md}} = \frac{6m_{\text{md}}}{\rho_L A_{\text{md}}}. \quad [39]$$

1. Droplet generation rate

The blowing number, which relates the intensity of the jet momentum to the properties of the liquid metal, is defined by the following expression^[67]:

$$N_B = \frac{\rho_G u_G^2}{2\sqrt{\sigma_L g \rho_L}} = \frac{\eta^2 p_d}{\sqrt{\sigma_L g \rho_L}} \quad \text{where} \quad \eta = \frac{u_G}{u_j}, \quad [40]$$

where u_G denotes the critical gas velocity, σ_L is the surface tension of the liquid steel, η is a constant, p_d is the dynamic pressure of the gas jet, and u_j is the axial velocity of the gas jet. The criterion for the Kelvin–Helmholtz instability, and thus the onset of droplet formation, is represented with a value of $N_B = 1$.^[67] The experimental results of other studies suggest that η is not independent of the lance height^[83–85] or the gas jet angle.^[86] Here, the variation of η as a function of the gas jet angle was treated in a similar fashion as by Alam *et al.*^[86] Making use of the concept of blowing number, Subagyo *et al.*^[67] proposed an empirical expression for droplet generation rate (\dot{m}_{md}) in the splashing cavity mode:

$$\frac{\dot{m}_{\text{md}}}{\dot{V}_{G,\text{lance}}} = \frac{(N_B)^{3.2}}{\left[2.6 \times 10^6 + 2.0 \times 10^{-4}(N_B)^{12}\right]^{0.2}} \quad R^2 = 0.97, \quad [41]$$

where $\dot{V}_{G,\text{lance}}$ is the volumetric gas flow rate through the top lance (Nm^3/s). As noted by Sarkar *et al.*^[87] and Rout *et al.*,^[88] Eq. [41] yields droplet generation rates which are considerably below the values estimated from plant data. According to Rout *et al.*,^[88] one reason for the discrepancy is the fact that Eq. [41] has been derived for conditions corresponding to room temperature. Similar to Rout *et al.*,^[88] Eq. [41] was modified such that the blowing number N_B and the volumetric gas flow rate $\dot{V}_{G,\text{lance}}$ are temperature corrected for the conditions at the point of impact:

$$\frac{\dot{m}_{\text{md}}}{\dot{V}'_{G,\text{lance}}} = \frac{(N'_B)^{3.2}}{\left[2.6 \times 10^6 + 2.0 \times 10^{-4}(N'_B)^{12}\right]^{0.2}}, \quad [42]$$

where N'_B is the modified blowing number and $\dot{V}'_{G,\text{lance}}$ is the modified volumetric gas flow rate. The modified

blowing number N_B' is obtained from Eq. [40] by employing the dynamic pressure at the point of impact. In this work, the dynamic pressure at the point of impact was calculated according to an experimental relationship proposed by Deo and Boom^[52]:

$$p_d = 230p_0 \left(\frac{h_{\text{lance}}}{d_t} \right). \quad [43]$$

The modified gas flow rate is calculated as follows^[88]:

$$\dot{V}'_{G,\text{lance}} = \frac{p_{G,\text{STP}}}{p_G} \frac{T_G}{T_{G,\text{STP}}} \dot{V}_{G,\text{lance}}, \quad [44]$$

where $p_{G,\text{STP}}$ is the standard pressure, p_G is the total pressure of the gas at the impact point, T_G is the temperature of the gas at the impact point and $T_{G,\text{STP}}$ is the standard temperature. Rout *et al.*^[88] suggested also that due to low lance height, the experiments conducted by Subagyo *et al.*^[67] did not actually correspond to splashing mode, but rather the penetrating mode of jet interaction, which is characterized by a lower droplet generation rate than in the splashing mode. For this reason, a dimensionless parameter J_{eff} was introduced similar to Sarkar *et al.*^[87] in order to calculate the effective droplet generation rate:

$$\dot{m}_{\text{md,eff}} = J_{\text{eff}} \times \dot{m}_{\text{md}}. \quad [45]$$

It should be noted that J_{eff} is essentially a fitting parameter, which is evaluated based on plant data.

2. Droplet size distribution

The size distribution of the metal droplets at their place of birth was determined according to Koria and Lange,^[89] who proposed a formulation based on the Rosin–Rammler–Sperling (RRS) function:

$$RF = (0.001) \left(\frac{d_{\text{md},i}}{d_{\text{limit}}} \right)^n, \quad [46]$$

where RF is the cumulative weight-fraction, d_{limit} is the limiting droplet diameter (which corresponds to $RF = 0.001$) and n is the distribution exponent. Experimental studies indicate that the parameter n is independent from the limiting diameter,^[89] maximum impact pressure of the gas jet^[89] and the blowing number.^[67] The reported values for the parameter n vary in a relatively wide range from 1.0 to 1.828.^[89,90] In this work, a value of $n = 1.26$ was taken from Koria and Lange,^[89] because it represents an arithmetic mean for a relatively large amount of data. For noncoalescing jets, the limiting diameter (in m) can be obtained from Koria and Lange^[91]:

$$d_{\text{limit}} = 5.513 \times 10^{-6} \times \left[10 \left(\frac{d_t^2}{h_{\text{lance}}^2} \right) p_{\text{amb}} \left(1.27 \frac{p_0}{p_{\text{amb}}} - 1 \right) \cos \theta \right]^{1.206}, \quad [47]$$

where p_0 and p_{amb} are the lance supply pressure (in Pa) and the ambient pressure (in Pa), respectively. This

expression suggests that droplet sizes increase with increasing lance supply pressure and decreasing lance height, and thus it appears to be in accordance with other studies.^[67,90,92] Modifying the expression presented by Deo *et al.*^[93] to a more general form, the mass fraction of size class i at place of birth can be obtained from

$$f_{\text{md},i} = -\ln(0.001) n RF \frac{d_{\text{md},i}^{n-1}}{d_{\text{limit}}^n}. \quad [48]$$

3. Residence time

The average residence time of the metal droplets is obtained from

$$\bar{t}_{\text{md}} = \frac{m_{\text{md}}}{\dot{m}_{\text{md}}}. \quad [49]$$

According to the results available in the literature, the average residence time of the droplets increases with an increasing top gas flow rate^[94] and decreasing droplet size.^[94,95] As shown by Urquhart and Davenport,^[96] the size distribution of the metal droplets in the emulsion is shifted toward smaller droplets than the distribution of the generated droplets. The residence time of an individual droplet in the emulsion can be defined as the ratio of the trajectory length to the average velocity.^[67] However, for the simplified setting considered in this work, it is more convenient to define the residence time of size class i through a constant κ as follows^[67]:

$$t_{\text{md},i} = \kappa \frac{h_{\text{em}}}{u_{\text{md},i}}, \quad [50]$$

where h_{em} is the height of the emulsion layer and $u_{\text{md},i}$ is the terminal velocity of size class i . Because the residence time approaches infinity as the droplet diameter approaches zero, the residence time was limited to $t_{\text{md},i} \leq 60$ seconds in order to avoid computational problems. The terminal velocity of the metal droplets in the emulsion was defined in three Reynolds ranges according to the equations proposed by Subagyo and Brooks.^[97] In the absence of suitable values, κ was taken here as unity. Moreover, it was assumed that all droplets of the same size class have the same residence time. The average thickness of the emulsion layer can be approximated from:

$$h_{\text{em}} = \frac{m_{\text{em}}}{A_{\text{slag}} \rho_{\text{em}}} = \frac{m_{\text{em}}}{(A_{\text{bath}} - n_{\text{lance}} \times \pi r_{\text{cav}}^2) \rho_{\text{em}}}, \quad [51]$$

where m_{em} is the mass of the emulsion, A_{slag} is the surface area of the top slag layer residing around the cavities, ρ_{em} is the density of the emulsion and A_{bath} is the cross-sectional area of the metal bath. The density of the slag-metal-slag emulsion is calculated according to Subagyo and Brooks^[97]:

$$\rho_{\text{em}} = \rho_L \phi_L + \rho_S (1 - \phi_L), \quad [52]$$

where ϕ_L denotes the volume fraction of metal droplets in emulsion, and is obtained from

$$\phi_L = \frac{V_L}{V_L + V_G + V_S} \quad \text{where} \quad V_G = \frac{\phi_G}{1 - \phi_G}(V_L + V_S), \quad [53]$$

where V_L , V_G , and V_S denote the volumes of metal, gas, and slag phases in emulsion, respectively. The volume-fraction of gas in the emulsion was solved numerically from the correlation proposed by Gou *et al.*^[98]:

$$\frac{\phi_G^2}{1 - \phi_G} = 0.91u_s^{0.57}, \quad [54]$$

where u_s is the superficial velocity. The superficial velocity was defined as the ratio of gas flow rate from the plume and cross-sectional area of the slag layer, *i.e.*, $u_s = \dot{V}_{G,\text{plume}}/A_{\text{slag}}$.

E. Mass- and Heat-Transfer Coefficients

The mass and heat-transfer coefficients were defined according to Eqs. [55] and [56], respectively.

$$\beta = \text{Sh} \frac{D}{L}, \quad [55]$$

$$\alpha = \text{Nu} \frac{\lambda}{L}, \quad [56]$$

where Sh is the Sherwood number, D is the mass diffusivity, L is the characteristic length, Nu is the Nusselt number, and λ is the heat conductivity. A detailed treatment of these parameters is provided in the following subsections.

1. Cavity interface

At the cavity interface, the cavity radius (r_{cav}) was employed as the characteristic length. The mass-transfer correlations employed for the gas jet were taken from Oeters.^[99] These correlations are based on the experimental data published by Lohe^[100] and can be represented as follows:

$$\text{Sh} = \begin{cases} 1.41\text{Re}^{0.51}\text{Sc}^{0.33} & \text{when } 2 \times 10^3 \leq \text{Re} \leq 3 \times 10^4 \\ 0.41\text{Re}^{0.75}\text{Sc}^{0.33} & \text{when } 3 \times 10^4 \leq \text{Re} \leq 2 \times 10^5 \end{cases}, \quad [57]$$

where Re is the Reynolds number and Sc is the Schmidt number. Similarly to Dogan *et al.*,^[101] the values of Re and Sc were defined in relation to the properties of the gas film at the impact surface:

$$\text{Re} = \frac{u_G r_{\text{cav}} \rho_G}{\mu_G}, \quad [58]$$

$$\text{Sc} = \frac{\mu_G}{\rho_G D_G}, \quad [59]$$

where u_G is the critical gas velocity, μ_G is the dynamic viscosity of the gas film, and ρ_G is the density of the

gas film. The critical gas velocity (u_G) is calculated from the free axial velocity of the gas jet (u_j). For the metal phase in contact with gas jet, the turbulent diffusion boundary layer thickness and the corresponding Sherwood number were defined according to Eqs. [60] and [61], respectively.^[99]

$$\delta_N = \sqrt{\frac{D_L \sigma_{\text{equiv}}}{0.41 \rho_L u_\tau^3}}, \quad [60]$$

$$\text{Sh} = \frac{r_{\text{cav}}}{2\delta_N}, \quad [61]$$

where u_τ is the turbulent shear stress velocity, and σ_{equiv} is the equivalent surface tension. The thickness of the thermal boundary layer (δ_{p_r}) can be obtained from Eq. [60] by replacing the mass diffusivity D_L with the ratio μ_L/ρ_L , *i.e.*, kinematic viscosity. As a first approximation, the mass-transfer coefficients of the slag species were similarly calculated as was done for the metal species, but making use of the properties of the slag species. Similar to Memoli *et al.*,^[102] the turbulent shear stress velocity was calculated on the basis of momentum transfer between the gas jet and the metal bath. Assuming that the axial velocity of the gas jet is zero at the bottom of the cavity, the turbulent shear stress velocity can be calculated as follows:

$$u_\tau = \sqrt{\frac{\rho_G}{\rho_L}} u_j. \quad [62]$$

The heat-transfer coefficients for gas, metal, and slag phases were derived from the mass-transfer correlations according to the analogs of heat and mass transfers by replacing the Sherwood number (Sh) and the Schmidt number (Sc) with the Nusselt number (Nu) and the Prandtl number (Pr), respectively.

2. Metal droplet interface

At the metal droplet interface, the mass- and heat-transfer coefficients were calculated by employing the Sauter mean diameter of the metal droplets ($d_{32,\text{md}}$) as the characteristic length. The mass-transfer coefficient mass of the gas phase in contact with the metal droplets can be calculated from the Steinberger and Treybal^[103] correlation, which accounts for the effects of both natural and forced convections:

$$\text{Sh} = \text{Sh}_0 + 0.347(\text{ReSc}^{1/2})^{0.62}, \quad [63]$$

$$\text{Sh}_0 = \begin{cases} 2 + 0.569(\overline{\text{GrSc}})^{1/4} & \text{for } \overline{\text{GrSc}} < 10^8 \\ 2 + 0.0254(\overline{\text{GrSc}})^{1/2}\text{Sc}^{0.244} & \text{for } \overline{\text{GrSc}} > 10^8 \end{cases}, \quad [64]$$

where $\overline{\text{Gr}}$ is the mean Grashof number. The mean Grashof number ($\overline{\text{Gr}}$), the Reynolds number (Re), and the Schmidt number (Sc) were defined as follows:

$$\overline{\text{Gr}} = \text{Gr}_M + \text{Gr}_H \left(\frac{\text{Sc}}{\text{Pr}} \right)^{1/2}, \quad [65]$$

$$\text{Re} = \frac{u_G d_{32,\text{md}} \rho_G}{\mu_G}, \quad [66]$$

$$\text{Sc} = \frac{\mu_G}{\rho_G D_G}, \quad [67]$$

where Gr_M is the Grashof number for mass transfer, Gr_H is the Grashof number for heat transfer, and Pr is the Prandtl number. Here, Gr_M , Gr_H , and Pr were defined according to Eqs. [68] through [70], respectively. It should be noted that the value of Gr_M depends on the species in question.

$$\text{Gr}_{M,i} = \frac{g \rho_G d_{32,\text{md}}^3 (y_{i,\text{md}}^* \rho_{G,\text{md}} - y_{i,\text{jet}} \rho_{G,\text{jet}})}{\mu_G^2}, \quad [68]$$

$$\text{Gr}_H = \frac{g \rho_G^2 d_{32,\text{md}}^3 (T_{\text{md}}^* - T_{\text{jet}})}{T_G \mu_G^2}, \quad [69]$$

$$\text{Pr} = \frac{c_{p,G} \mu_G}{\lambda_G}, \quad [70]$$

where $c_{p,G}$ is the specific heat capacity of the gas phase, and λ_G is the heat conductivity of the gas phase. The heat-transfer coefficient was calculated by means of Eqs. [63] and [64] by replacing Sh , $\overline{\text{Gr}}$, and Sc with Nu , Gr_H , and Pr , respectively. It is known that mass transfer within small metal droplets takes place almost entirely by diffusion, while larger droplets may exhibit uninhibited circulatory flow.^[99,104] In this work, it was assumed that only creeping laminar circulation takes place within the metal droplets. Therefore, the mass-transfer coefficient can be calculated according to the Kronig and Brink^[105] solution, which can be expressed in terms of the Sherwood number as follows^[106]:

$$\text{Sh} = \frac{32 \sum_{i=1}^{\infty} A_i^2 \lambda_i \exp(-16\lambda_i \text{Fo}_M)}{3 \sum_{i=1}^{\infty} A_i^2 \exp(-16\lambda_i \text{Fo}_M)}, \quad [71]$$

where Fo_M is the Fourier number for mass transfer. The first seven values for the parameters A_i and λ_i were taken from the literature^[107] and provide a sufficient convergence. Despite its limited range of theoretical applicability, experimental studies have shown that the Kronig and Brink solution gives a reasonably good prediction of the mass-transfer coefficient even at Reynolds numbers well above those corresponding to creeping flow.^[108] Employing the average residence time of the metal droplets (\bar{t}_{md}) as the characteristic

time, the Fourier number for mass transfer can be defined according to

$$\text{Fo}_M = \frac{4D_L \bar{t}_{\text{md}}}{d_{32,\text{md}}^2}. \quad [72]$$

The corresponding Fourier number for heat transfer (Fo_H) is obtained from Eq. [72] by replacing mass diffusivity with thermal diffusivity. Thus, the heat-transfer coefficient for the metal droplets is obtained by replacing Sh and Fo_M with Nu and Fo_H , respectively. The mass transfer in the slag phase surrounding the metal droplets was calculated according to Eq. [73], which is valid for fluid spheres in creeping flow.^[109]

$$\begin{aligned} \text{Sh} &= 0.65 \left(\frac{\mu_S}{\mu_S + \mu_L} \right)^{1/2} \text{Re}^{1/2} \text{Sc}^{1/2} \\ &= 0.65 \left(\frac{\mu_S}{\mu_S + \mu_L} \right)^{1/2} \left(\frac{\rho_S \bar{u}_{\text{md}} d_{32,\text{md}}}{\mu_S} \right)^{1/2} \left(\frac{\mu_S}{\rho_S D_S} \right)^{1/2}, \end{aligned} \quad [73]$$

where \bar{u}_{md} is the average terminal velocity of the metal droplets in the emulsion. The heat-transfer coefficient for the slag phase in contact with the metal droplets was obtained using the analogs of heat and mass transfers by replacing Sh and Sc with Nu and Pr , respectively.

F. Thermodynamic Properties

All the thermodynamic properties were defined at the composition and temperature of the reaction interface in question. The equilibrium constants are defined by

$$K = \exp\left(-\frac{\Delta G^\circ}{RT^*}\right) \quad \text{where} \quad \Delta G^\circ = \Delta H^\circ - T^* \Delta S^\circ, \quad [74]$$

where R is the gas constant; T^* is the temperature of the reaction interface; and ΔG° , ΔH° , and ΔS° are the changes in Gibbs free energy, enthalpy, and entropy of reaction, respectively. The reaction enthalpy and reaction entropy were calculated according to Eqs. 75 and 76, respectively.

$$\Delta H^\circ = \sum_{i=1}^n v_i H_i^\circ, \quad [75]$$

$$\Delta S^\circ = \sum_{i=1}^n v_i S_i^\circ, \quad [76]$$

where v_i , H_i° and S_i° are the stoichiometric coefficient, enthalpy and entropy of species i . The values of H_i° and S_i° at temperature T were calculated as follows:

$$H^\circ(T) = H_{298.15}^\circ + \int_{298.15}^T C_p dT + H_{tr,T}^\circ + H_{dis}^\circ, \quad [77]$$

$$S^\circ(T) = S_{298.15}^\circ + \int_{298.15}^T \frac{C_p}{T} dT + S_{tr,T}^\circ + S_{dis}^\circ, \quad [78]$$

where $H_{298.15}^\circ$ is the enthalpy at 298.15 K (25 °C), C_p is the molar heat capacity, H_{tr}° is the total enthalpy of phase transformations from 298.15 K (25 °C) to T , H_{dis}° is the enthalpy of dissolution, $S_{298.15}^\circ$ is the entropy at 298.15 K (25 °C), S_{tr}° is the total entropy of phase transformations from 298.15 K (25 °C) to T , and S_{dis}° is the entropy of dissolution. The enthalpies H° and entropies S° correspond to the following standard states: the Henrian standard state for the species dissolved in the metal bath, and the Raoultian standard states for the gas and slag species. For the dissolved species, the relevant values of H_{dis}° and S_{dis}° were obtained from Sigworth and Elliott,^[110] while for the gas and slag species, H_{dis}° and S_{dis}° were set to zero. The molar heat capacity at temperature T is solved from the Shomate equation^[111]:

$$C_p = A + B \cdot 10^{-3} T + C \cdot 10^5 T^{-2} + D \cdot 10^{-6} T^2, \quad [79]$$

where A , B , C , and D are fitting parameters applicable to a certain temperature interval. A comprehensive database of the Shomate equation parameters was taken from HSC Chemistry.^[111] The partial pressures of the gaseous species can be calculated from the ideal gas law based on the total gas pressure at the reaction interface.

The Henrian activity coefficients of the species in the liquid metal phase were calculated by means of the Unified Interaction Parameter (UIP) formalism^[112]:

$$\ln \gamma_i^H = \ln \frac{\gamma_i^R}{\gamma_i^\circ} = -0.5 \sum_{j=1}^n \sum_{k=1}^n \varepsilon_j^k x_j^* x_k^* + \sum_{j=1}^n \varepsilon_i^j x_j^*, \quad [80]$$

where γ_i^H is the Henrian activity coefficient of species i , γ_i^R is the Raoultian activity coefficient of species i , γ_i° is the activity coefficient of species i at infinite dilution, ε is the first-order molar interaction parameter, and x^* is the molar fraction at the reaction interface. The employed first-order molar interaction parameters are given in Table II.

The activity coefficients of the slag species were calculated according to the model employed by Wei and Zhu.^[21] The Raoultian activity coefficients of FeO, Cr₂O₃, MnO, and SiO₂ are given by Eqs. [81] through [84], respectively.

$$\begin{aligned} \log_{10} \gamma_{FeO}^R &= \frac{\varepsilon_1}{T^*} (x_{CaO}^* + x_{MgO}^*) (x_{SiO_2}^* + 0.25x_{AlO_{1.5}}^*) \\ &+ \frac{\varepsilon_2}{T^*} x_{MnO}^* (x_{SiO_2}^* + 0.45x_{CrO_{1.5}}^*) \\ &+ \frac{\varepsilon_3}{T^*} x_{AlO_{1.5}}^* x_{SiO_2}^* + \frac{\varepsilon_4}{T^*} x_{MnO}^* x_{AlO_{1.5}}^* \\ &+ \frac{\varepsilon_5}{T^*} x_{CrO_{1.5}}^* x_{SiO_2}^*, \end{aligned} \quad [81]$$

$$\begin{aligned} \log_{10} \gamma_{Cr_2O_3}^R &= \log_{10} \gamma_{FeO}^R - \frac{\varepsilon_6}{T^*} (x_{CaO}^* + x_{MgO}^*) - \frac{\varepsilon_7}{T^*} x_{MnO}^* \\ &- \frac{\varepsilon_5}{T^*} x_{SiO_2}^*, \end{aligned} \quad [82]$$

Table II. Employed First-Order Molar Interaction Parameters in Liquid Iron at 1873 K (1600 °C)

ε_i^j	Fe	Cr	Mn	Si	C
Fe	—	—	—	—	—
Cr	—	0.00475 ^[113]	—	1.73 ^[114]	-4.9 ^[115]
Mn	—	—	-0.642 ^[113]	-3.3 ^[115]	-1.9 ^[115]
Si	—	1.73 ^[114]	-3.3 ^[115]	12.0 ^[115]	9.8 ^[115]
C	—	-4.9 ^[115]	-1.9 ^[115]	9.8 ^[115]	13 ^[115]
O	—	-4.84 ^[116]	-4.7 ^[116]	-7.1 ^[116]	-20 ^[116]
N	—	-9.8 ^[115]	-4.5 ^[115]	6.1 ^[115]	7.2 ^[115]
Ni	—	-0.0027 ^[115]	-1.8 ^[115]	1.2 ^[115]	2.4 ^[115]
Al	—	—	—	7.0 ^[115]	5.3 ^[115]
S	—	-2.2 ^[113]	-5.9 ^[113]	9.2 ^[113]	6.3 ^[113]
ε_i^j	O	N	Ni	Al	S
Fe	—	—	—	—	—
Cr	-4.84 ^[116]	-9.8 ^[115]	-0.0027 ^[115]	—	-2.2 ^[113]
Mn	-4.7 ^[116]	-4.5 ^[115]	-1.8 ^[115]	—	-5.9 ^[113]
Si	-7.1 ^[116]	6.1 ^[115]	1.2 ^[115]	7.0 ^[115]	9.2 ^[113]
C	-20.0 ^[116]	7.2 ^[115]	2.4 ^[115]	5.3 ^[115]	6.3 ^[113]
O	-10.7 ^[116]	4.0 ^[110]	2.4 ^[116]	-434.2 ^[110]	-17.1 ^[110]
N	4.0 ^[110]	0.75 ^[115]	1.6 ^[115]	1.6 ^[115]	1.4 ^[110]
Ni	2.4 ^[116]	1.6 ^[115]	0.17 ^[110]	—	0 ^[116]
Al	-434.2 ^[110]	1.6 ^[115]	—	5.5 ^[110]	4.4 ^[110]
S	-17.1 ^[110]	1.4 ^[110]	0 ^[116]	4.4 ^[110]	-5.6 ^[113]

$$\log_{10} \gamma_{\text{MnO}}^{\text{R}} = \log_{10} \gamma_{\text{FeO}}^{\text{R}} - \frac{\varepsilon_2}{T^*} \left(x_{\text{SiO}_2}^* + 0.45x_{\text{CrO}_{1.5}}^* \right) - \frac{\varepsilon_4}{T^*} x_{\text{AlO}_{1.5}}^* \quad [83]$$

$$\log_{10} \gamma_{\text{SiO}_2}^{\text{R}} = \log_{10} \gamma_{\text{FeO}}^{\text{R}} - \frac{\varepsilon_1}{T^*} \left(x_{\text{CaO}}^* + x_{\text{MgO}}^* \right) - \frac{\varepsilon_2}{T^*} x_{\text{MnO}}^* - \frac{\varepsilon_3}{T^*} x_{\text{AlO}_{1.5}}^* - \frac{\varepsilon_5}{T^*} x_{\text{CrO}_{1.5}}^* \quad [84]$$

where $\varepsilon_1, \dots, \varepsilon_7$ are the interaction coefficients of the model. Table III shows the interaction coefficients reported by Wei and Zhu^[21] for early and later periods of refining. In this work, the coefficients applicable for the early period of refining were employed. Similar to Wei and Zhu,^[21] it was assumed that $a_{\text{Cr}_2\text{O}_3}^{\text{R}} = 1$ if the interfacial Cr_2O_3 content is greater than the maximum solubility of Cr_2O_3 in the slag.

G. Physical Properties

The physical properties of the metal and slag phases were estimated at the temperature of the reaction interface, while the properties of the gas phase were

defined at gas film temperature, which was approximated as^[117]

$$T_{\text{G}} = 0.5 \times (T^* + T_{\text{jet}}), \quad [85]$$

where T^* is the temperature of reaction interface, and T_{jet} is the temperature of the gas jet. The effective mass diffusivity was defined for each species in the metal phase as the interdiffusivity in liquid iron, while only one effective diffusivity value was assigned for the gas and slag phases. Where possible, the temperature dependency of the mass diffusivity of solutes in liquid iron was described by an Arrhenius type relationship.^[118] In order to account for the effects of pressure and temperature, the mass diffusivity of the gaseous species was treated similar to Järvinen *et al.*^[29]:

$$D_{\text{G}} = D_{\text{G,eff}} \times \left(\frac{T_{\text{G}}}{T_{\text{ref}}} \right)^{1.5} \left(\frac{p_{\text{ref}}}{p_{\text{G}}} \right), \quad [86]$$

where $D_{\text{G,eff}}$ is the effective mass diffusivity at T_{ref} and p_{ref} , T_{ref} is the reference temperature, p_{ref} is the reference pressure, and p_{G} is the total gas pressure. The pressure changes in the gas jet are small enough to be neglected,^[72] and hence the total gas pressure

Table III. Interaction Coefficients of the Slag Model^[21]

Stage	Interaction Coefficients						
	ε_1	ε_2	ε_3	ε_4	ε_5	ε_6	ε_7
Early Period of Refining	3540	1475	1068	36	593	1594	664
Later Period of Refining	4130	1720	1246	42	692	1859	774

Table IV. Employed Models and Parameters for Physical Properties

Property	Employed Value or Method	Notes	References
ρ_{L}	temperature function	stainless steel grade 304	119
ρ_{G}	ideal gas law	—	—
ρ_{S}	partial molar volume method	—	120
μ_{L}	temperature function	stainless steel grade 304	119
μ_{G}	Wilke's equation	gas mixture	121
$\mu_{i,\text{G}}$	Chapman–Enskog equation	gas species	122–124
$\mu_{\text{S(l)}}$	Forsbacka <i>et al.</i> model	liquid slag	125
$\mu_{\text{S,rel}}$	Thomas equation	effect of solid particles	126
$D_{\text{L,eff}}$	interdiffusion coefficients	values in liquid iron	118
$D_{\text{G,eff}}$	$0.185 \times 10^{-4} \text{ m}^2/\text{s}$	O_2 –CO binary at 273.0 K (–0.15 °C) and 101325 Pa	127
$D_{\text{S,eff}}$	$5.0 \times 10^{-10} \text{ m}^2/\text{s}$	estimated value at 1873 K (1600 °C)	128
λ_{L}	temperature function	stainless steel grade 304	119
λ_{G}	Mason–Saxena equation	gas mixture	122
$\lambda_{i,\text{G}}$	Eucken equation	gas species	122
λ_{S}	1.0 W/(m K)	estimated value	—
$c_{\text{p,L}}$	weight-averaged value	liquid metal mixture	—
$c_{\text{p,G}}$	weight-averaged value	gas mixture	—
$c_{\text{p,S}}$	weight-averaged value	slag mixture	—
$c_{\text{p},i}$	Shomate equation	species	111
σ_{L}	1.5 N/m	estimated value	129

was taken as equal to the atmospheric pressure at both reaction interfaces. The treatment of other physical properties is summarized in Table IV along with their corresponding references.

During decarburization, the top slag consists of a molten slag phase saturated with chromium oxide and a

solid chromium oxide phase.^[130] For this reason, it is necessary to consider the effect of solid particles on the viscosity of the top slag. The viscosity of the liquid part ($\mu_{S(l)}$) was calculated using the viscosity model proposed by Forsbacka *et al.*,^[125] which is an extension of the modified Urbain model^[131] for the $\text{Al}_2\text{O}_3\text{-CaO-CrO-Cr}_2\text{O}_3\text{-FeO-MgO-SiO}_2$ system. The effective viscosity of the top slag was determined as relative to the viscosity of the liquid slag phase:

$$\mu_S = \mu_{S(l)}\mu_{S,\text{rel}} \quad [87]$$

The relative viscosity $\mu_{S,\text{rel}}$ was calculated according to the equation proposed by Thomas.^[126] Figure 5 provides a comparison of the Thomas^[126] equation with other relative viscosity equations available in the literature.^[132–138] With the exception of the Einstein equation,^[132] the equations produce similar results up to a solid volume fraction of 0.3, but begin to diverge as the solid volume fraction approaches unity. The solid volume fraction was calculated as a function of Cr_2O_3 content as shown in the second part of this work.^[44]

H. Numerical Solution

The objective of the numerical solution routine is to minimize the error in free variables, while minimizing

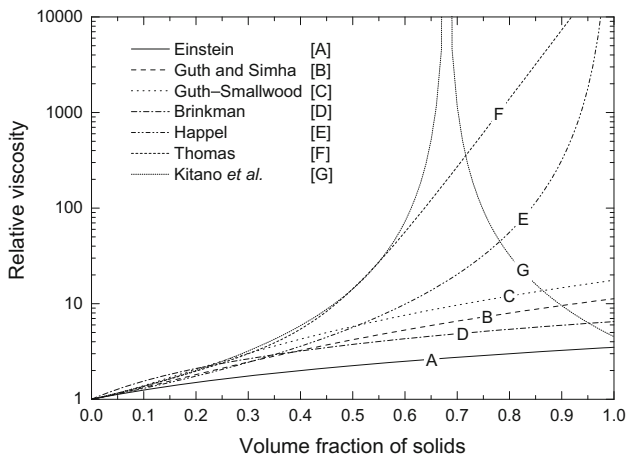


Fig. 5—Calculated relative viscosity as a function of the volume fraction of solids.^[126,132–138]

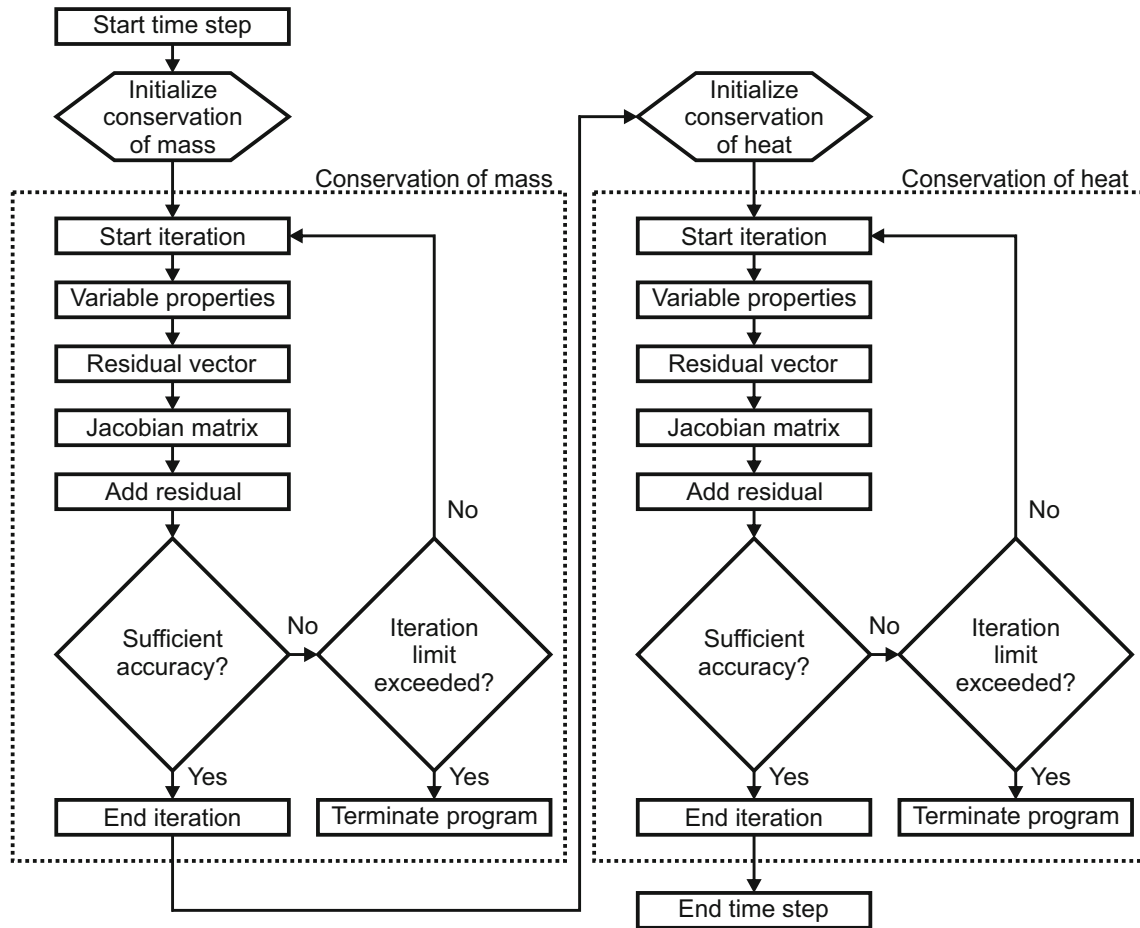


Fig. 6—Flowchart of the reaction model.

the error in thermodynamic equilibrium at the reaction interfaces. The thermodynamic equilibrium equations at the reaction interface and the mass transfer onto and from the interface are solved simultaneously. However, conservations of mass and heat are solved successively. Using small time steps, this does not cause significant inaccuracy, but greatly improves the numerical stability. The flowchart of the model is shown in Figure 6.

The numerical solutions of both iteration loops are obtained by Newton's method, which approximates the solution by its tangent line.^[139] For a set of nonlinear equations, the Newton's method can be expressed as follows^[50]:

$$\mathbf{J}\Delta\mathbf{x} = -\mathbf{f}, \quad [88]$$

where \mathbf{J} is the Jacobian matrix of the system with respect to all free variables, $\Delta\mathbf{x}$ is the correction vector, and \mathbf{f} is the residual vector, which approaches zero asymptotically during the iteration. The system of linear equations defined by Eq. [88] is solved by Gauss–Jordan elimination method. During iteration, the vector of free variables is updated similar to the relaxed Newton's method. The calculation procedure is repeated until the numerical error is sufficiently small or the maximum number of iterations is exceeded. The error in the residual vector \mathbf{f} is measured using the L^2 -norm, which is the Euclidian length of the correction vector:

$$\|\Delta\mathbf{x}\|_2 = \sqrt{\sum_i \Delta x_i^2}. \quad [89]$$

As stated earlier, one of the main assumptions of the model is that the reaction interfaces reach their mass-transfer constrained equilibrium composition at every instant. During the numerical solution, the interfacial composition asymptotically approaches the composition dictated by the equilibrium constants, provided that the forward reaction rate coefficients (k_f) are sufficiently large. In order to assess the fulfillment of the equilibrium assumption, the concept of equilibrium number is introduced:

$$E = \left| 1 - \frac{Q}{K} \right|, \quad [90]$$

where Q and K denote the reaction quotient and the equilibrium constant, respectively. The reaction quotient is defined as follows:

$$Q = \frac{\sum_p a_p^{y_p}}{\sum_r a_r^{y_r}}, \quad [91]$$

where p and r denote reaction products and reactants, respectively. By definition, $Q = K$ at equilibrium. Because $Q \rightarrow K$ as $k_f \rightarrow \infty$, it follows that $E \rightarrow 0$ as $k_f \rightarrow \infty$. Owing to these properties, the equilibrium number provides a practical measure of the relative fulfillment of the equilibrium assumption. As a preliminary setting, the maximum allowed error was set to $E = 0.1$ pct for all the studied reactions. During numerical solution, the forward reaction rate

coefficients are increased periodically until the equilibrium numbers of all the reactions are below the maximum allowed error. A typical calculation time per time step is in the order of few seconds using a desk-top PC (3.4 GHz).

III. CONCLUSIONS

The objective of this work was to develop a fast numerical model for the reactions that occur during top-blowing in the AOD process. More specifically, the aim was to create a model that considers reactions both between the top-blown gas and the metal bath and between metal droplets and top slag. Employing the categorization proposed by Ding *et al.*,^[41] the model derived in this work can be classified as a complex process mechanism model, because it emphasizes the local thermodynamic equilibrium and local heat and mass-transfer characteristics. In the second part of this work,^[44] the model is validated with heats from a full size AOD vessel. In the future, the combined top- and side-blowing stage of the AOD process can be simulated as a combination of the top-blowing model derived in this work and the side-blowing model proposed earlier by Järvinen *et al.*^[29]

ACKNOWLEDGMENTS

This research has been conducted within the framework of the DIMECC SIMP research program. The funding for this work from Outokumpu Stainless Oy, the Finnish Funding Agency for Technology and Innovation (TEKES), the Graduate School in Chemical Engineering (GSCE), the Academy of Finland (Projects 258319 and 26495), the Finnish Foundation for Technology Promotion, the Finnish Science Foundation for Economics and Technology, and the Tauno Tönning Foundation is gratefully acknowledged. The first author thanks Professor Herbert Pfeifer for the possibility to conduct part of the research work at RWTH Aachen University. In addition, the authors are grateful to Professor Rauf Hürman Eriç, Kevin Christmann, and Tim Haas for their valuable comments on this manuscript.

NOMENCLATURE

SYMBOLS

a	Activity
A	Surface area (m ²)
A_i	Parameter of the Kronig–Brink solution
C_p	Molar heat capacity at constant pressure (J/(mol K))

c_p	Specific heat capacity at constant pressure (J/(kg K))
d_t	Nozzle throat diameter (m)
d_{limit}	Fineness parameter of the RRS distribution (m)
$d_{32,\text{md}}$	Sauter mean diameter of the metal droplets (m)
D	Diffusion coefficient (m^2/s)
f_i	Mass fraction of size class i at place of birth
\mathbf{f}	Residual vector
g	Standard gravity (m/s^2)
ΔG°	Change in standard Gibbs free energy of reaction (J/mol)
ΔG_{tot}	Change in total Gibbs free energy (J/mol)
h_{cav}	Depth of the cavity (m)
h_{lance}	Distance of the top lance from the surface of the metal bath (m)
H°	Standard enthalpy (J/mol)
ΔH°	Change in standard reaction enthalpy (J/mol)
\mathbf{J}	Jacobian matrix
J_{eff}	Droplet generation rate multiplication factor
k_f	Forward reaction rate coefficient
K	Equilibrium constant
L	Characteristic length (m)
m	Mass (kg)
\dot{m}_{md}	Metal droplet generation rate (kg/s)
$\dot{m}_{\text{md,eff}}$	Effective metal droplet generation rate (kg/s)
M	Molar mass (kg/mol)
n_{lance}	Number of exit ports in a nozzle
n	Distribution exponent of the RRS distribution
p	Partial pressure
p_{cav}	Arc length of the cavity (m)
p_{amb}	Ambient pressure (Pa)
p_0	Stagnation pressure at upstream part of the top lance (Pa)
r_{cav}	Top radius of the cavity (m)
R	Gas constant (J/(mol K))
R''	Reaction rate ($\text{kg}/(\text{m}^2 \text{ s})$)
R^2	Correlation coefficient
RF	Cumulative weight fraction
S°	Standard entropy (J/(mol K))
ΔS°	Change in standard reaction entropy (J/(mol K))
$t_{\text{md},i}$	Residence time of metal droplet size class i (s)
\bar{t}_{md}	Average residence time of the metal droplets (s)
T	Temperature (K)
T^*	Interfacial temperature (K)
u_G	Critical gas velocity (m/s)
u_j	Axial velocity of the gas jet (m/s)
$u_{\text{md},i}$	Terminal velocity of metal droplet size class i (m/s)
\bar{u}_{md}	Average terminal velocity of the metal droplets (m/s)
u_τ	Turbulent shear stress velocity (m/s)
\dot{V}_G	Volumetric gas flow rate (Nm^3/s)
\dot{V}'_G	Modified volumetric gas flow rate (Nm^3/s)
x	Molar fraction
X	Cation fraction
$\Delta \mathbf{x}$	Correction vector
y	Mass fraction

y^*	Interfacial mass fraction
$ \Delta \mathbf{x} _2$	l^2 -norm

GREEK SYMBOLS

α	Heat-transfer coefficient ($\text{W}/(\text{m}^2 \text{ K})$)
α	Interaction energy between cations (J)
β	Mass-transfer coefficient (m/s)
γ	Activity coefficient
γ°	Activity coefficient at infinite dilution
δ_{N}	Thickness of the diffusion boundary layer (m)
δ_{Pr}	Thickness of the thermal boundary layer (m)
ε	First-order molar interaction parameter
η	Constant
$\bar{\eta}_{\text{H}}$	Average microkinetic efficiency of heat transfer
$\bar{\eta}_{\text{M}}$	Average microkinetic efficiency of mass transfer
θ	Inclination angle of each nozzle relative to lance axis (deg)
κ	Constant
λ	Heat conductivity ($\text{W}/(\text{m}\cdot\text{K})$)
λ_i	Parameter of the Kronig–Brink solution
μ	Dynamic viscosity (Pa·s)
ν	Stoichiometric coefficient
$\bar{\nu}$	Mass-based stoichiometric coefficient
π	Mathematical constant
ρ	Density (kg/m^3)
σ	Surface tension (N/m)
ϕ	Volume fraction

DIMENSIONLESS NUMBERS

E	Equilibrium number
Fo_{H}	Fourier number for heat transfer
Fo_{M}	Fourier number for mass transfer
Gr	Mean Grashof number
Gr_{H}	Grashof number for heat transfer
Gr_{M}	Grashof number for mass transfer
N_{B}	Blowing number
N'_{B}	Modified blowing number
Nu	Nusselt number
Sc	Schmidt number
Sh	Sherwood number
Pr	Prandtl number
Re	Reynolds number

SUBSCRIPTS AND SUPERSCRIPTS

cav	Cavity
bath	Metal bath
em	Gas–metal–slag emulsion
G	Gas phase
H	Henrian standard state
in	Gas flow into the system

jet	Gas jet
L	Liquid metal phase
md	Metal droplet
out	Gas flow out of the system
plume	Gas plume
R	Raoultian standard state
rel	Relative
S	Slag phase
STP	Standard temperature and pressure according to the DIN 1343 standard ^[49] : 273.15 K (0 °C) and 101325 Pa
slag	Top slag
(l)	Liquid state
(s)	Solid state

INDICES

<i>i</i>	Size class
<i>i</i>	Species
<i>n</i>	Number of species
<i>r</i>	Number of reactions
ψ	Phase
ω	Reaction interface

REFERENCES

- B.V. Patil, A.H. Chan, and R.J. Choulet: in *The Making, Shaping and Treating of Steel. Steel Making and Refining*, 11th ed., R.J. Fruehan, ed., The AISE Steel Foundation, Pittsburgh, 1998, pp. 715–41.
- J.-H. Wei, J.-C. Ma, Y.-Y. Fan, N.-W. Yu, S.-L. Yang, S.-H. Xiang, and D.-P. Zhu: *Ironmak. Steelmak.*, 1999, vol. 26, pp. 363–71.
- P. Ternstedt, A. Tilliander, P.G. Jönsson, and M. Iguchi: *ISIJ Int.*, 2010, vol. 50, pp. 663–67.
- J.-H. Wei, H.-L. Zhu, H.-B. Chi, and H.-J. Wang: *ISIJ Int.*, 2010, vol. 50, pp. 26–34.
- J.-H. Wei, Y. He, and G.-M. Shi: *Steel Res. Int.*, 2011, vol. 82, pp. 693–702.
- H. Gorges, W. Pulvermacher, W. Rubens, and H.-A. Dierstein: *Stahl Eisen*, 1979, vol. 99, pp. 1310–12.
- P.R. Scheller and F.-J. Wahlers: *ISIJ Int.*, 1996, vol. 36, pp. S69–72.
- H.-L. Zhu, J.-H. Wei, G.-M. Shi, J.-H. Shu, Q.-Y. Jiang, and H.-B. Chi: *Steel Res. Int.*, 2007, vol. 78, pp. 305–10.
- T. Watanabe and T. Tohge: *Tetsu-to-Hagané*, 1973, vol. 59, pp. 1224–36.
- S. Asai and J. Szekely: *Metall. Trans.*, 1974, vol. 5, pp. 651–57.
- J. Szekely and S. Asai: *Metall. Trans.*, 1974, vol. 5, pp. 1573–80.
- R.J. Fruehan: *Ironmak. Steelmak.*, 1976, vol. 3, pp. 153–58.
- T. Ohno and T. Nishida: *Tetsu-to-Hagané*, 1977, vol. 63, pp. 2094–99.
- T. Deb Roy and D.G.C. Robertson: *Ironmak. Steelmak.*, 1978, vol. 5, pp. 198–206.
- T. Deb Roy, D.G.C. Robertson, and J.C.C. Leach: *Ironmak. Steelmak.*, 1978, vol. 5, pp. 207–10.
- A.E. Semin, A.P. Pavlenko, T. Andzhum, and E.A. Shuklina: *Steel USSR*, 1983, vol. 13, pp. 95–97.
- T. Tohge, Y. Fujita, and T. Watanabe: *Proceedings of the 4th Process Technology Conference*, Chicago, IL, 1984, pp. 129–36.
- P. Sjöberg: Doctoral thesis, Royal Institute of Technology, Stockholm, Sweden, 1994.
- J. Reichel and J. Szekely: *Iron Steelmaker*, 1995, vol. 22, pp. 41–48.
- M. Görnerup and P. Sjöberg: *Ironmak. Steelmak.*, 1999, vol. 26, pp. 58–63.
- J.-H. Wei and D.-P. Zhu: *Metall. Mater. Trans. B*, 2002, vol. 33B, pp. 111–19.
- J.-H. Wei and D.-P. Zhu: *Metall. Mater. Trans. B*, 2002, vol. 33B, pp. 121–27.
- N. Kikuchi, K. Yamaguchi, Y. Kishimoto, S. Takeuchi, and H. Nishikawa: *Tetsu-to-Hagané*, 2002, vol. 88, pp. 32–39.
- B. Deo and V. Srivastava: *Mater. Manuf. Process.*, 2003, vol. 18, pp. 401–08.
- B. Kleimt, R. Lichterbeck, and C. Burkat: *Stahl Eisen*, 2007, vol. 127, pp. 35–41.
- G.-M. Shi, J.-H. Wei, H.-L. Zhu, J.-H. Shu, Q.-Y. Jiang, and H.-B. Chi: *Steel Res. Int.*, 2007, vol. 78, pp. 311–17.
- M. Järvinen, A. Kärnä, and T. Fabritius: *Steel Res. Int.*, 2009, vol. 80, pp. 429–36.
- J.-H. Wei, Y. Cao, H.-L. Zhu, and H.-B. Chi: *ISIJ Int.*, 2011, vol. 51, pp. 365–74.
- M.P. Järvinen, S. Pislä, A. Kärnä, T. Ikäheimonen, P. Kupari, and T. Fabritius: *Steel Res. Int.*, 2011, vol. 82, pp. 638–49.
- S.E. Pislä, M.P. Järvinen, A. Kärnä, T. Ikäheimonen, T. Fabritius, and P. Kupari: *Steel Res. Int.*, 2011, vol. 82, pp. 650–57.
- D.R. Swinbourne, T.S. Kho, B. Blanpain, S. Arnout, and D.E. Langberg: *Miner. Process. Extr. Metall.*, 2012, vol. 121, pp. 23–31.
- N.A.I. Andersson, A. Tilliander, L.T.I. Jönsson, and P.G. Jönsson: *Steel Res. Int.*, 2012, vol. 83, pp. 1039–52.
- N.A.I. Andersson, A. Tilliander, L.T.I. Jönsson, and P.G. Jönsson: *Steel Res. Int.*, 2013, vol. 84, pp. 169–77.
- N.A.I. Andersson, A. Tilliander, L.T.I. Jönsson, and P.G. Jönsson: *Ironmak. Steelmak.*, 2013, vol. 40, pp. 390–97.
- N.A.I. Andersson, A. Tilliander, L.T.I. Jönsson, and P.G. Jönsson: *Ironmak. Steelmak.*, 2013, vol. 40, pp. 551–58.
- V.-V. Visuri, M. Järvinen, P. Sulasalmi, E.-P. Heikkinen, J. Savolainen, and T. Fabritius: *ISIJ Int.*, 2013, vol. 53, pp. 603–12.
- V.-V. Visuri, M. Järvinen, J. Savolainen, P. Sulasalmi, E.-P. Heikkinen, and T. Fabritius: *ISIJ Int.*, 2013, vol. 53, pp. 613–21.
- R.J. Fruehan: *Metall. Trans. B*, 1975, vol. 6, pp. 573–78.
- Y. Tang, T. Fabritius, and J. Härkki: *Steel Res. Int.*, 2004, vol. 75, pp. 373–81.
- J. Riipi, T. Fabritius, E.-P. Heikkinen, P. Kupari, and A. Kärnä: *ISIJ Int.*, 2009, vol. 49, pp. 1468–73.
- R. Ding, B. Blanpain, P.T. Jones, and P. Wollants: *Metall. Mater. Trans. B*, 2000, vol. 31B, pp. 197–206.
- Y. Uchida, N. Kikuchi, K. Yamaguchi, Y. Kishimoto, S. Takeuchi, and H. Nishikawa: *Proceedings of the 2nd International Conference on Process Development in Iron and Steelmaking*, Luleå, Sweden, 2004, pp. 69–78.
- J.-H. Wei and Y. Li: *Steel Res. Int.*, 2015, vol. 86, pp. 189–211.
- V.-V. Visuri, M. Järvinen, A. Kärnä, P. Sulasalmi, E.-P. Heikkinen, P. Kupari, and T. Fabritius: *Metall. Mater. Trans. B.*, DOI:10.1007/s11663-017-0960-5.
- M. Järvinen, V.-V. Visuri, S. Pislä, A. Kärnä, P. Sulasalmi, E.-P. Heikkinen, and T. Fabritius: *Mater. Sci. Forum*, 2013, vol. 762, pp. 236–41.
- M. Järvinen, V.-V. Visuri, E.-P. Heikkinen, A. Kärnä, P. Sulasalmi, C. De Blasio, and T. Fabritius: *ISIJ Int.*, 2016, vol. 56, pp. 1543–52.
- Z. Song: Doctoral thesis, Royal Institute of Technology, Stockholm, Sweden, 2013.
- Y. Tang, T. Fabritius, and J. Härkki: *Appl. Math. Model.*, 2005, vol. 29, pp. 497–514.
- Deutsches Institut für Normung e.V.: DIN 1343, Referenzzustand, Normzustand, Normvolumen; Begriffe und Werte, DIN1343, Referenzzustand, Normzustand, Normvolumen; Begriffe und Werte, 1990.
- R. Taylor and R. Krishna: *Multicomponent Mass Transfer*, Wiley, New York, 1993, p. 126.
- R.I.L. Guthrie: *Engineering in Process Metallurgy*, Clarendon Press, Oxford, 1989, p. 282.
- B. Deo and R. Boom: *Fundamentals of Steelmaking Metallurgy*, Prentice Hall International, Hertfordshire, 1993, p. 170/176.
- H.-J. Odenthal, U. Falkenreck, and J. Schlüter: *Proceedings of the European Conference on Computational Fluid Dynamics*, Egmond aan Zee, The Netherlands, 2006, p. 21.
- N. Molloy: *J. Iron Steel Inst.*, 1970, vol. 208, pp. 943–50.

55. S. Sabah and G. Brooks: *ISIJ Int.*, 2014, vol. 54, pp. 836–44.
56. X. Zhou, M. Ersson, L. Zhong, J. Yu, and P. Jönsson: *Steel Res. Int.*, 2014, vol. 85, pp. 273–81.
57. S.K. Sharma, J.W. Hlinka, and D.W. Kern: *Iron Steelmaker*, 1977, vol. 24, pp. 7–18.
58. D. Nakazono, K.-I. Abe, M. Nishida, and K. Kurita: *ISIJ Int.*, 2004, vol. 44, pp. 91–99.
59. F.R. Cheslak, J.A. Nicholls, and M. Sichel: *J. Fluid Mech.*, 1969, vol. 36, pp. 55–63.
60. S.N. Krivoshapko and V.N. Ivanov: *Encyclopedia of Analytical Surfaces*, Springer, Cham, 2015, p. 110.
61. C.K. Lee, J.H. Neilson, and A. Gilchrist: *Iron Steel Int.*, 1977, vol. 50, pp. 175–84.
62. C.K. Lee, J.H. Neilson, and A. Gilchrist: *Ironmak. Steelmak.*, 1977, vol. 4, pp. 329–37.
63. S.C. Koria and K.W. Lange: *Steel Res.*, 1987, vol. 58, pp. 421–26.
64. K.W. Lange and S.C. Koria: *Wechselwirkung zwischen Sauerstoffstrahl und Roheisenschmelze beim Sauerstoffaufblasverfahren.*, Publ. Wiss. Film. Techn. Wiss./Naturw., Ser. 8, No. 9, Institut für den Wissenschaftlichen Film, Göttingen, Germany, 1983, Film D 1386.
65. J.-H. Wei and L. Zeng: *Steel Res. Int.*, 2012, vol. 83, pp. 1053–70.
66. S.C. Koria: Doctoral thesis, RWTH Aachen University, Aachen, Germany, 1981.
67. Subagyo, G.A. Brooks, K.S. Coley, and G.A. Irons: *ISIJ Int.*, 2003, vol. 43, pp. 983–89.
68. E. Schürmann and K. Rosenbach: *Arch. Eisenhüttenwes.*, 1973, vol. 44, pp. 761–68.
69. W. Rubens: Doctoral thesis, Clausthal University of Technology, Clausthal-Zellerfeld, Germany, 1988.
70. K. Koch, W. Münchberg, H. Zörcher, and W. Rubens: *Stahl Eisen*, 1992, vol. 112, pp. 91–99.
71. T.X. Zhu, K.S. Coley, and G.A. Irons: *Metall. Mater. Trans. B*, 2012, vol. 43B, pp. 751–57.
72. E.T. Turkdogan: *Chem. Eng. Sci.*, 1966, vol. 21, pp. 1133–44.
73. N. Standish and Q.L. He: *ISIJ Int.*, 1989, vol. 29, pp. 455–61.
74. I. Hahn: Doctoral thesis, RWTH Aachen University, Aachen, Germany, 1999.
75. A. Feiterna, D. Huin, F. Oeters, P.-V. Riboud, and J.-L. Roth: *Steel Res.*, 2000, vol. 71, pp. 61–69.
76. Z. Han and L. Holappa: *ISIJ Int.*, 2003, vol. 43, pp. 292–97.
77. Z. Han and L. Holappa: *ISIJ Int.*, 2003, vol. 43, pp. 1698–704.
78. S.C. Koria and K.W. Lange: *Ironmak. Steelmak.*, 1983, vol. 10, pp. 160–68.
79. K.-Y. Lee, H.-G. Lee, and P.C. Hayes: *ISIJ Int.*, 1998, vol. 38, pp. 1242–47.
80. H.W. Meyer, W.F. Porter, G.C. Smith, and J. Szekely: *J. Met.*, 1968, vol. 20, pp. 35–42.
81. G. Lindstrand, P.G. Jönsson, and A. Tilliander: *Proceedings of the ISIJ-VDEh-Jernkontoret Joint Symposium*, Osaka, Japan, 2013, pp. 106–13.
82. A. Nordquist, A. Tilliander, K. Grönlund, G. Runnsjö, and P. Jönsson: *Ironmak. Steelmak.*, 2009, vol. 36, pp. 421–31.
83. W. Kleppe and F. Oeters: *Arch. Eisenhüttenwes.*, 1977, vol. 48, pp. 139–43.
84. S. Sabah, M. Alam, G. Brooks, and J. Naser: *4th International Conference on Process Development in Iron and Steelmaking*, Luleå, Sweden, 2012, pp. 125–34.
85. S. Sabah and G. Brooks: *Metall. Mater. Trans. B*, 2015, vol. 46B, pp. 863–72.
86. M. Alam, G. Irons, G. Brooks, A. Fontana, and J. Naser: *ISIJ Int.*, 2011, vol. 51, pp. 1439–47.
87. S. Sarkar, P. Gupta, S. Basu, and N.B. Ballal: *Metall. Mater. Trans. B*, 2015, vol. 46, pp. 961–76.
88. B. K. Rout, G. Brooks, Subagyo, M. A. Rhamdhani and Z. Li: *Metall. Mater. Trans. B*, 2016, vol. 47, pp. 3350–3361.
89. S.C. Koria and K.W. Lange: *Metall. Trans. B*, 1984, vol. 15, pp. 109–16.
90. C. Cicutti, M. Valdez, T. Pérez, J. Petroni, A. Gómez, R. Donayo, and L. Ferro: *Proceedings of the 6th International Conference on Motel Slags, Fluxes and Salts*, Stockholm, Sweden—Helsinki, Finland, 2000, pp. 1–17.
91. S.C. Koria and K.W. Lange: *Ironmak. Steelmak.*, 1986, vol. 13, pp. 236–40.
92. S.-Y. Kitamura and K. Okohira: *Tetsu-to-Hagané*, 1990, vol. 76, pp. 199–206.
93. B. Deo, A. Karamcheti, A. Paul, P. Singh, and R.P. Chhabra: *ISIJ Int.*, 1996, vol. 36, pp. 658–66.
94. Q.L. He and N. Standish: *ISIJ Int.*, 1990, vol. 30, pp. 356–61.
95. G. Brooks, Y. Pan, Subagyo, and K. Coley: *Metall. Mater. Trans. B*, 2005, vol. 36B, pp. 525–35.
96. R.C. Urquhart and W.G. Davenport: *Can. Metall. Q.*, 1973, vol. 12, pp. 507–16.
97. Subagyo and G.A. Brooks: *ISIJ Int.*, 2002, vol. 42, pp. 1182–84.
98. H. Gou, G.A. Irons, and W.-K. Lu: *Metall. Mater. Trans. B*, 1996, vol. 27, pp. 195–201.
99. F. Oeters: *Metallurgie der Stahlherstellung*, p. 162/174/337, Verlag Stahleisen mbH, Düsseldorf, Germany, 1989.
100. H. Lohe: *Fortschr. -Ber. VDI-Z.*, 1967, Ser. 3, No. 15, pp. 1–59.
101. N. Dogan, G.A. Brooks, and M.A. Rhamdhani: *ISIJ Int.*, 2011, vol. 51, pp. 1102–09.
102. F. Memoli, C. Mapelli, P. Ravaneli, and M. Corbella: *ISIJ Int.*, 2004, vol. 44, pp. 1342–49.
103. R.L. Steinberger and R.E. Treybal: *AICHe J.*, 1960, vol. 6, pp. 227–32.
104. K.W. Lange: *Arch. Eisenhüttenwes.*, 1971, vol. 42, pp. 233–41.
105. R. Kronig and J.C. Brink: *Appl. Sci. Res.*, 1951, vol. 2, pp. 142–154.
106. D. Colombet, D. Legendre, A. Cockx, and P. Guiraud: *Int. J. Heat Mass Trans.*, 2013, vol. 67, pp. 1096–1105.
107. P.M. Heertjes, W.A. Holve, and H. Talsma: *Chem. Eng. Sci.*, 1954, vol. 3, pp. 122–142.
108. R. Clift, J.R. Grace, and M.E. Weber: *Bubbles, Drops and Particles*, Academic Press, New York, 1978.
109. P.H. Calderbank: *Chem. Eng.*, 1967, vol. 45, pp. 209–33.
110. G.K. Sigworth and J.F. Elliott: *Met. Sci.*, 1974, vol. 8, pp. 298–310.
111. Outotec Oyj: *HSC Chemistry 8*, 2015.
112. A.D. Pelton and C.W. Bale: *Metall. Trans. A*, 1986, vol. 17, pp. 1211–15.
113. A.V. Alpatov and S.N. Paderin: *Russ. Metall.*, 2010, vol. 2010, pp. 557–64.
114. W.E. Slye and R.J. Fruehan: *Proceedings of the 57th Electric Furnace Conference*, Pittsburgh, PA, 1999, pp. 401–12.
115. S. Ueno, Y. Waseda, K.T. Jacob, and S. Tamaki: *Steel Res.*, 1988, vol. 59, pp. 474–83.
116. K.V. Malyutin and S.N. Paderin: *Russ. Metall.*, 2007, vol. 2007, pp. 545–51.
117. J. Szekely and N.J. Themelis: *Rate Phenomena in Process Metallurgy*, Wiley, New York, 1971, p. 459.
118. K. Nagata, Y. Ono, T. Ejima, and T. Yamamura: in *Handbook of Physico-chemical Properties at High Temperatures*, Y. Kawai and Y. Shiraiishi, eds., The Iron and Steel Institute of Japan, Tokyo, Japan, 1988, pp. 181–204.
119. IAEA: *Thermophysical Properties of Materials for Nuclear Engineering: A Tutorial and Collection of Data*, International Atomic Energy Agency, Vienna, Austria, 2008, p. 169.
120. B.J. Keene and K.C. Mills: in *Verein Deutscher Eisenhüttenleute: Slag Atlas*, 2nd ed., Verlag Stahleisen GmbH, Düsseldorf, Germany, 1995, pp. 313–48.
121. C.R. Wilke: *J. Chem. Phys.*, 1950, vol. 18, pp. 517–19.
122. R.B. Bird, W.E. Stewart, and E.N. Lightfoot: *Transport Phenomena*, Wiley, Singapore, 1960, p. 23.
123. G.H. Geiger and D.R. Poirier: *Transport Phenomena in Metallurgy*, Addison-Wesley Publishing Company, Reading, 1973, p. 11.
124. L.D. Cloutman: *A Database of Selected Transport Coefficients for Combustion Studies*, Lawrence Livermore National Laboratory, Livermore, 1993, p. 5.
125. L. Forsbacka, L. Holappa, A. Kondratiev, and E. Jak: *Steel Res. Int.*, 2007, vol. 78, pp. 676–84.
126. D.G. Thomas: *J. Colloid Sci.*, 1965, vol. 20, pp. 267–77.
127. C.R. Wilke and C.Y. Lee: *Ind. Eng. Chem.*, 1955, vol. 47, pp. 1253–57.
128. K.C. Mills: in *Verein Deutscher Eisenhüttenleute: Slag Atlas*, 2nd ed., Verlag Stahleisen GmbH, Düsseldorf, Germany, 1995, pp. 541–56.
129. C.F. Wuppermann: Doctoral thesis, RWTH Aachen University, Aachen, Germany, 2013.

130. O. Wijk: in *Principles of Metal Refining*, T.A. Engh, ed., Oxford University Press, Oxford, United Kingdom, 1992, pp. 280–301.
131. G. Urbain: *Steel Res.*, 1987, vol. 58, pp. 111–16.
132. A. Einstein: *Ann. Phys.*, 1906, vol. 19, pp. 289–306.
133. E. Guth and R. Simha: *Kolloid Z.*, 1936, vol. 74, pp. 266–75.
134. E. Guth: *J. Appl. Phys.*, 1945, vol. 16, pp. 20–25.
135. H.M. Smallwood: *J. Appl. Phys.*, 1944, vol. 15, pp. 758–66.
136. H.C. Brinkman: *J. Chem. Phys.*, 1952, vol. 20, p. 571.
137. J. Happel: *J. Appl. Phys.*, 1957, vol. 28, pp. 1288–92.
138. T. Kitano, T. Kataoka, and T. Shirota: *Rheol. Acta*, 1981, vol. 20, pp. 207–09.
139. E. Kreyszig, H. Kreyszig, and E.J. Norminton: *Advanced Engineering Mathematics*, 10th ed., Wiley, Hoboken, 2011, p. 909.